CrossMark

# Utilizing 2D Electrical Resistivity Tomography and Very Low Frequency Electromagnetics to Investigate the Hydrogeology of Natural Cold Springs Near Virginia City, Southwest Montana

MOHAMED A. KHALIL,[1] (iD) ANDREW BOBST,[2] and JESSE MOSOLF[2]

*Abstract*—Virginia City, Montana, is located in the northern Rocky Mountains of the United States. Two natural springs supply the city's water; however, the source of that water is poorly understood. The springs are located on the east side of the city, on the edge of an area affected by landslides. 2D electric resistivity tomography (ERT) and very low frequency electromagnetics (VLF-EM) were used to explore the springs and landslides. Two intersecting 2D resistivity profiles were measured at each spring, and two VLF profiles were measured in a landslide zone. The inverted 2D resistivity profiles at the springs reveal high resistivity basalt flows juxtaposed with low resistivity volcanic ash. The VLF profiles within the landslide show a series of fracture zones in the basalt, which are interpreted to be a series of landslide scarps. Results show a strong correlation between the inferred scarps and local topography. This study provides valuable geological information to help understand the source of water to the springs. The contact between the fractured basalt and the ash provides a sharp contrast in permeability, which causes water to flow along the contact and discharge at outcrop. The fracture zones along the scarps in the landslide deposits provide conduits of high secondary permeability to transmit water to the springs. The fracture zones near the scarps may also provide targets for municipal supply wells.

**Key words:** 2D resistivity, VLF, springs, Montana.

## 1. Introduction

Virginia City is one of southwest Montana's oldest and most celebrated mining districts that now attracts more than 300,000 tourists annually, greatly straining the area's limited water resources. Two cold springs (known as spring 1, and spring 2) emanating from a hillside east of Virginia City have long served as the municipal water supply; however, the source of the springs' water is poorly understood. As such, there is uncertainty regarding how the springs may be affected by climatic variations, and groundwater development in the area. To better characterize the hydrogeology of the springs we employed 2D Electric Resistivity Tomography (ERT) and very low frequency electromagnetics (VLF-EM) methods.

In recent years, the use of 2D and 3D ERT has increased, covering a large spectrum of hydrogeological, archaeological, environmental and engineering applications (e.g. Wynn and Grosz (2000), Madsen et al. (2001), Manheim et al. (2001), Dahlin et al. (2002), Tonkov and Loke (2006), Forquet and French (2012)). In the field of geophysical investigation of springs, Qarqori et al. (2012) used ERT methods to study a fractures network around Bittit Spring, Middle Atlas, Morocco. The ERT data allowed them to propose a theory for the hydrological behavior of water from the Tabular Middle Atlas and the Saïs Basins at the Bittit Spring, which considers both horizontal flows through stratification joints or karst and through subvertical fractures. Rizzo et al. (2004) used ERT methods for mapping active faults and to estimate the subsurface resistivity patterns of the High Agri Valley basin (Southern Italy). The Agri Valley contains a complex Quaternary fault network of the Apennine chain and its geometry, the location and dip of the master fault and the tectonic evolution was controversial.

The VLF-EM method (bandwidths of 15–30 kHz) has been used to identify preferred flow paths in the subsurface (e.g. Moeck et al. 2003). Because of the easy operation of the instrument, speed of field survey and low operation cost, VLF-EM is very

[1] Department of Geophysical Engineering, Montana Tech of the University of Montana, Butte, USA. E-mail: mkhalil@mtech.edu
[2] Montana Bureau of Mines and Geology, Butte, USA.

Birkhäuser

suitable for rapid preliminary surveys and has been widely used in many geophysical studies since the 1960s (McNeill and Labson 1991, Monteiro Santos et al. 2006, Khalil et al. 2010).

Results from this study help to characterize the hydrogeology of the springs feeding Virginia City's municipal water supply and will potentially aid the exploration of additional ground water sources in the area. Here we report on the results from collecting 2D ERT profiles near the springs and VLF-EM profiles within the landslide deposits.

## 2. Geological Setting

Virginia City is located within the northern Rocky Mountains at an elevation of ∼ 1767 m above mean sea level and is situated in a topographic low between two major mountain ranges: the Tobacco Root Mountains to the north (up to 3200 m-amsl), and the Greenhorn Range to the south (up to 2900 m-amsl) (Fig. 1). The precipitation in Virginia City averages 389 mm/year, and the mean monthly temperatures vary from − 4.8 °C in December to 18.4 °C in July. The average annual temperature is 6.2 °C (Western Regional Climate Center, 2017).

The oldest rocks in the study area are Archean gneiss, amphibolite, marble, quartzite, and small bodies of ultramafic rock (see Ruppel and Liu 2004). These rocks generally exhibit a penetrative metamorphic foliation and lineation and are deformed by several sets of folds (Cordua 1973). Proterozoic pegmatite (∼ 1.6 Ga; James 1990) and diabase (∼ 1.4–1.1 Ga; Wooden et al. 1978) intrude the
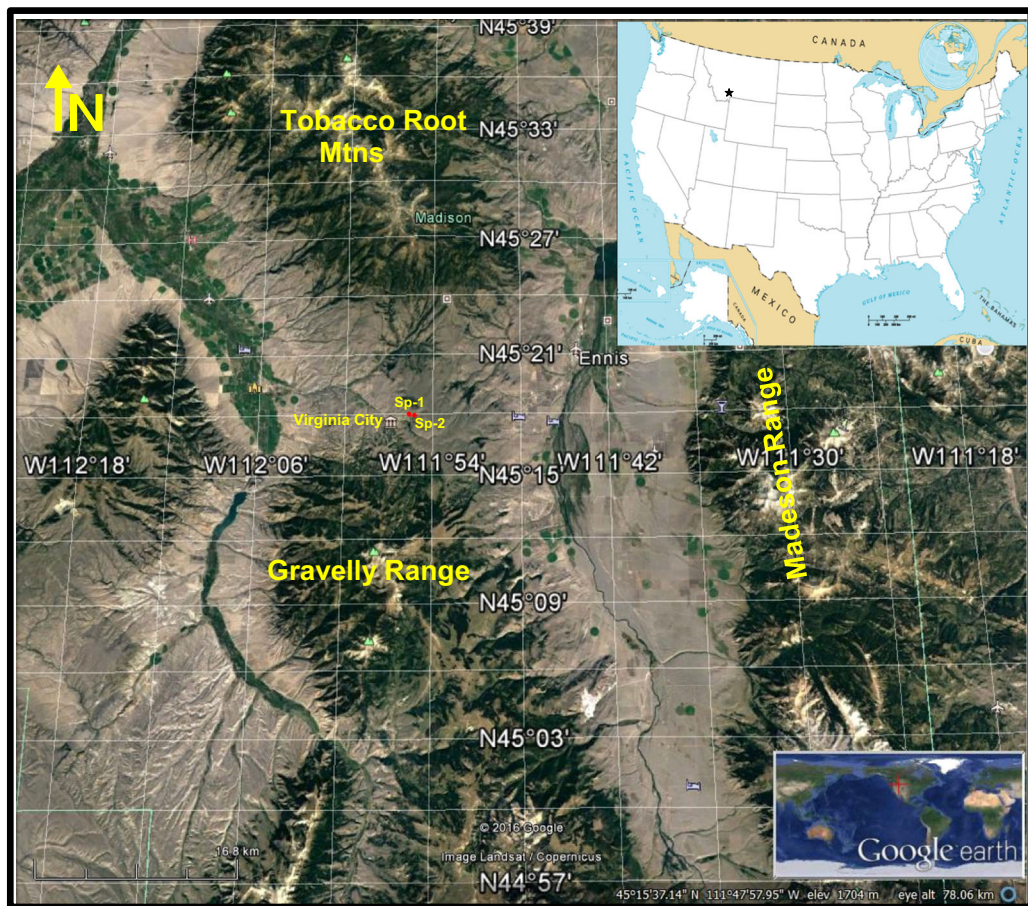


Figure 1
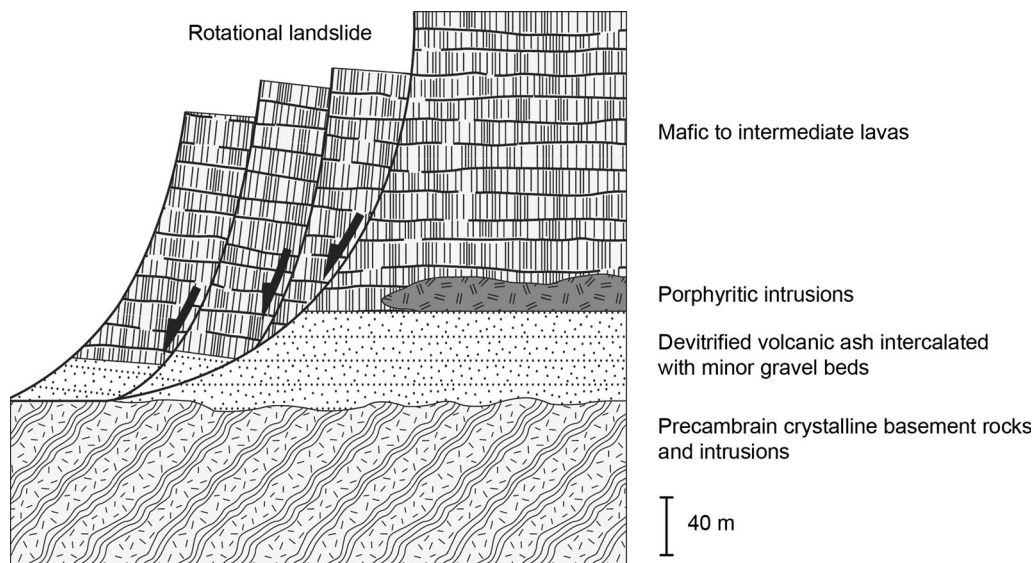Location map of Virginia City. Google Earth

Figure 2
Generalized stratigraphy of the study area

Archean crystalline basement and are not significantly foliated or metamorphosed. Many of the Proterozoic intrusions appear to have been emplaced along brittle faults and fractures.

A sequence of Tertiary volcanic deposits and intercalated gravel with a composite thickness of approximately 300 m unconformably rest on the Archean basement rocks (Ruppel and Liu 2004). A recessive, poorly exposed ash-flow tuff occurs near the stratigraphic base of the Tertiary volcanic pile and is locally intercalated with coarse gravels (Fig. 2). The tuff is composed of fine-grained ash that has been devitrified to clay; deposits commonly contain accidental clasts derived from the underlying basement rocks. A $\sim$ 200 m thick sequence of mafic-to-intermediate lava flows overlies the tuff and gravel deposits, commonly forming high-standing mesas. Lavas are aphanitic to porphyritic, containing sparse phenocrysts of plagioclase, olivine, and augite, and quartz xenocrysts. Autobrecciation and vertical columnar joints are common. Rare porphyritic intrusions contain phenocrysts of plagioclase, biotite, and hornblende. Previously reported K–Ar ages for volcanic intervals in the Virginia City area range from $51.1 \pm 1.9$ to $32.7 \pm 1.4$ Ma (Marvin et al. 1974; Kellogg and Williams 2006).

The Tertiary volcanic units are prone to mass wasting and consequentially, several large rotational and translational landslide deposits rim the high-standing volcanic mesa immediately north of Virginia City. The main surface of rupture of individual landslide deposits is commonly rooted in the basal devitrified tuff. Spring 1 (45.29888287°N 111.9271716°W) is located on the edge of a large landslide complex, and at the contact between the basalt and tuff. Spring 2 (45.29925022°N 111.9191184°W) is also located at the contact between the basalt and tuff, but these units appear to be in place (i.e. they are not part of a landslide).

Quaternary alluvial deposits occurring in Alder Gulch host placer gold and silver that has been extensively mined. These deposits generally consist of rounded to well-rounded pebbles to boulders derived from the Archean crystalline basement. Placer gold and silver was likely concentrated from the weathering of dominantly NE- and NW-trending quartz veins hosted in local Archean basement rocks (Ruppel and Liu 2004).

The most notable tectonic structure in the study area is the northwest-striking Virginia City fault zone inferred to underlie the modern Alder Gulch stream drainage. The slip history for this fault is not well
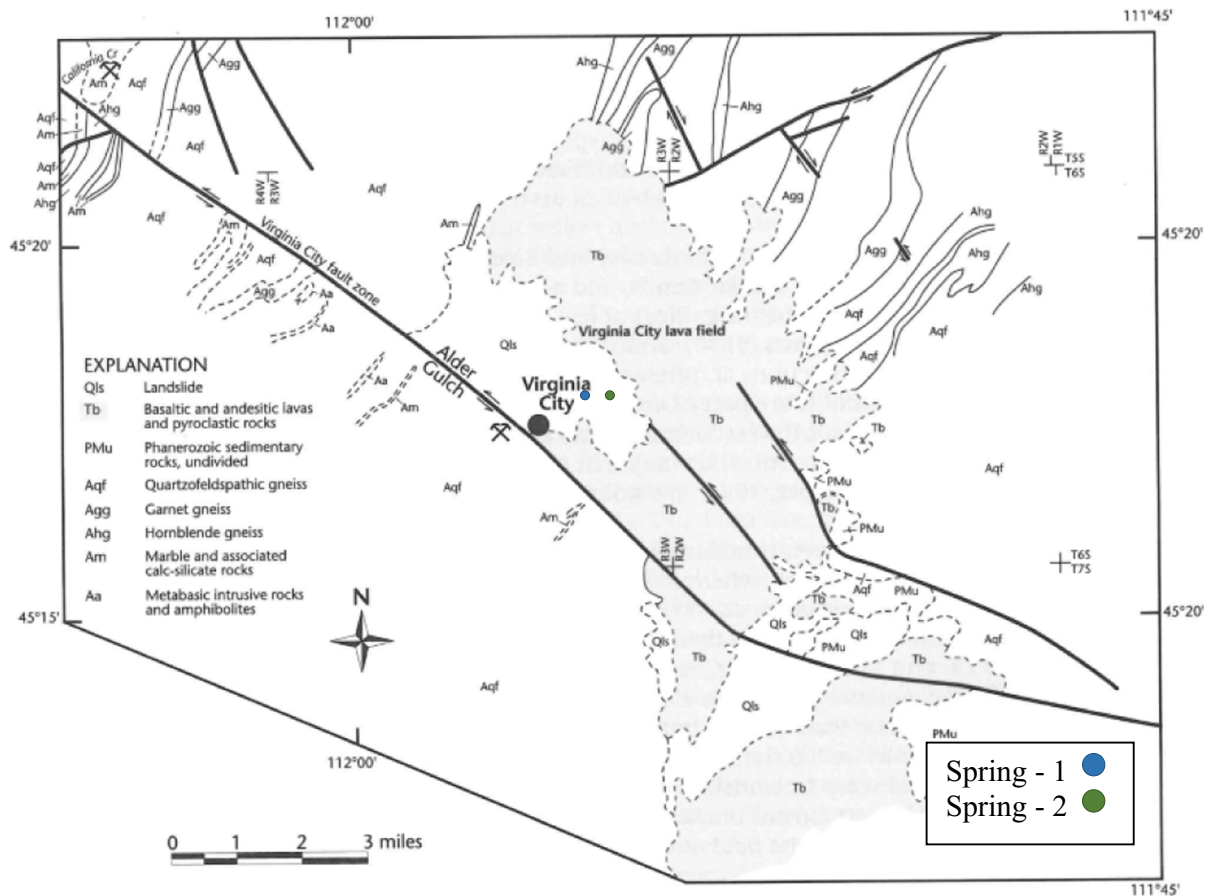
Figure 3
Simplified geologic map of the Virginia City area, modified from Ruppel and Liu (2004). Green and blue dots show the approximate locations of the springs investigated in this study

constrained, but fault movement is hypothesized to have begun in the Early Proterozoic (James 1990), and has since moved repeatedly. Ruppel and Liu (2004) interpreted the Virginia City fault zone to be a major sinistral strike-slip fault, displacing the Tertiary volcanic rocks over 9 km. Subsidiary fault strands strike northwest, subparallel to the Virginia City fault zone (Fig. 3).

### 2.1. Survey Area Description

Spring 1 is located on the edge of a relatively flat area that accommodates Virginia City's municipal water infrastructure including conduit, treatment, and a water tank. A man-made trench filled with gravel

and a pipe directs the spring water to a spring box, and from there it is routed either to the treatment and storage facility, or to a nearby surface discharge point. The area below the spring is gently sloped and underlain by clayey soils. The hill above the spring is composed basaltic volcanic rocks.

Spring 2 is located along a stretch of north–south trending dirt road, constructed along a break in slope. Steeply inclined slopes occur east of the road in an area underlain by basaltic volcanic rocks. The area west of the road is relatively flat and underlain by clay rich soils. In-place basalts and a layer of breccia observed in the roadcut (Fig. 4) indicate that Site 2 (Spring 2) is not underlain by a landslide deposit.

The landslide area—where VLF-1 and VLF-2 were measured—consists of grass-covered terrain

Figure 4
Road cut on Site 2 (the scale is approximate)

with little infrastructure. A large fence runs east–west across this site. Pressure ridges at this site are visible in satellite imagery.

## 3. Methodology

We used two geophysical methods in this study: 2D Electrical Resistivity Tomography (ERT), and

Very Low Frequency Electromagnetics (VLF-EM). The coordinates and elevations of all measured points were acquired using a Leica GPS, which is a Real Time Kinematic (RTK) satellite navigation system with centimeter-level precision.

### 3.1. I- 2D ERT

The ERT method is known for its versatility, with the ability to function in regions with high relief topography. ERT is based on a conventional four-electrode resistivity system, where electric current is injected via two current electrodes and the potential difference is measured between the two potential electrodes. At each spring we measured two inter-secting profiles, approximately centered at the spring (Fig. 5). Each profile was 200 m long with 10-m minimum electrode spacing. We used a Wenner array for its high signal strength, and high sensitivity to vertical resistivity changes (Loke 1995). Using a Wenner array with a large potential electrode spacing requires less sensitivity from the resistivity meter (Burger et al. 2006). The data were collected using a SYSCALR2- resistivity meter, from IRIS-instruments. A 250-W DC–DC converter was used for
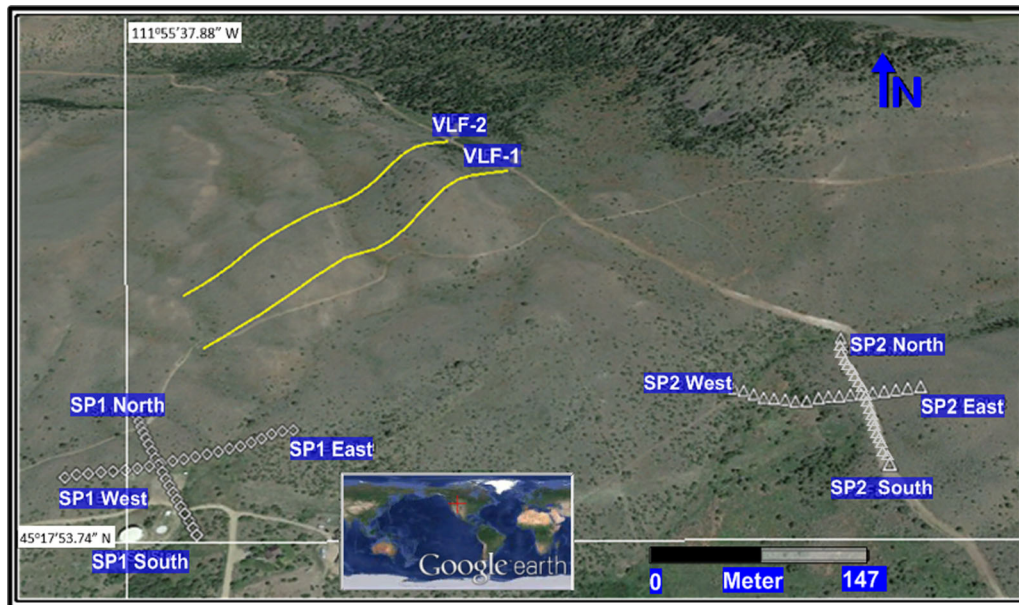


Figure 5
Survey site with survey lines

converting energy from a 12-V battery, and to inject electrical current through the ground. A series of twenty-one electrodes were used in the array, and salt water was used to decrease the contact resistance between the electrodes and the soil.

Electrode spacing was increased with each new data line allowing us to look deeper into the subsurface. The first line of data started with a 10-m electrode spacing. This spacing was increased by 10-m increments for each data line until the electrode spacing reached a maximum of 60-m. Contact resistance was checked for each measurement for quality control. This process was repeated for each of the four profiles.

### 3.2. II-VLF-EM

The theory behind VLF-EM and its application to geological and hydrogeological problems have been broadly discussed in the literature (e.g. McNeill and Labson, 1991). VLF is an electromagnetic method that uses electromagnetic radiation from military navigation radio transmitters operating in the VLF frequency band (15–30 kHz). The transmitted radio signals have two forms: ground waves, and waves guided by both the solid earth and the conducting ionosphere. In the presence of an electrically conductive, steeply dipping, elongated (2D) target, the primary field will induce secondary eddy currents. The VLF-EM instrument measures only the vertical (Hz) and the horizontal (Hy) components of the magnetic field. A scalar tipper $B$ given by $Hz = B$ Hy can be defined for each measuring point. Over a 2D Earth, the tipper $B$ value varies along a profile and shows the strongest variations near resistivity contrasts. The real and imaginary components (or in-phase and quadrature components, respectively) of the tipper $B$ values are usually expressed as a percentage. The difference between resistive and conductive anomalies is based on the polarity of the in-phase and out-of-phase components. The two components have the same polarity for a resistive anomaly, but for a conductive anomaly the out-of-phase component changes in polarity and shape.

VLF-EM data in this study were collected using a WADI (ABEM) system, along two parallel profiles (Fig. 5) approximately oriented NE–SW. Each profile extends 500 m in length. The distance between the profiles was 150 m and the station spacing was 5 m. A transmitter frequency of 24.7 kHz was found to
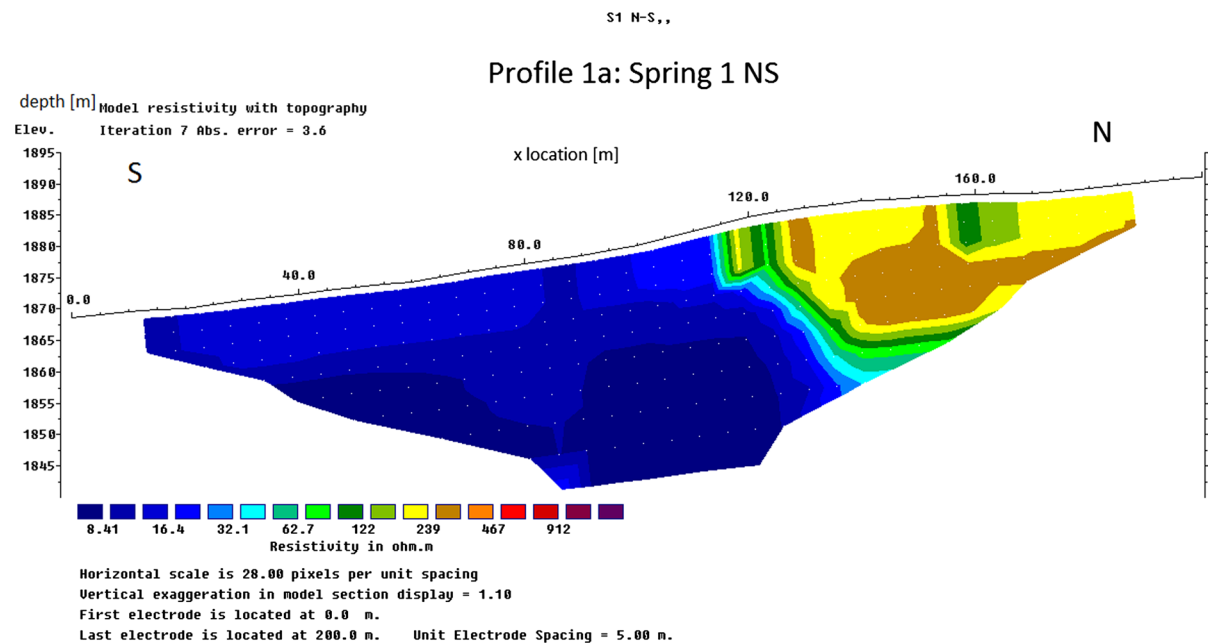


Figure 6
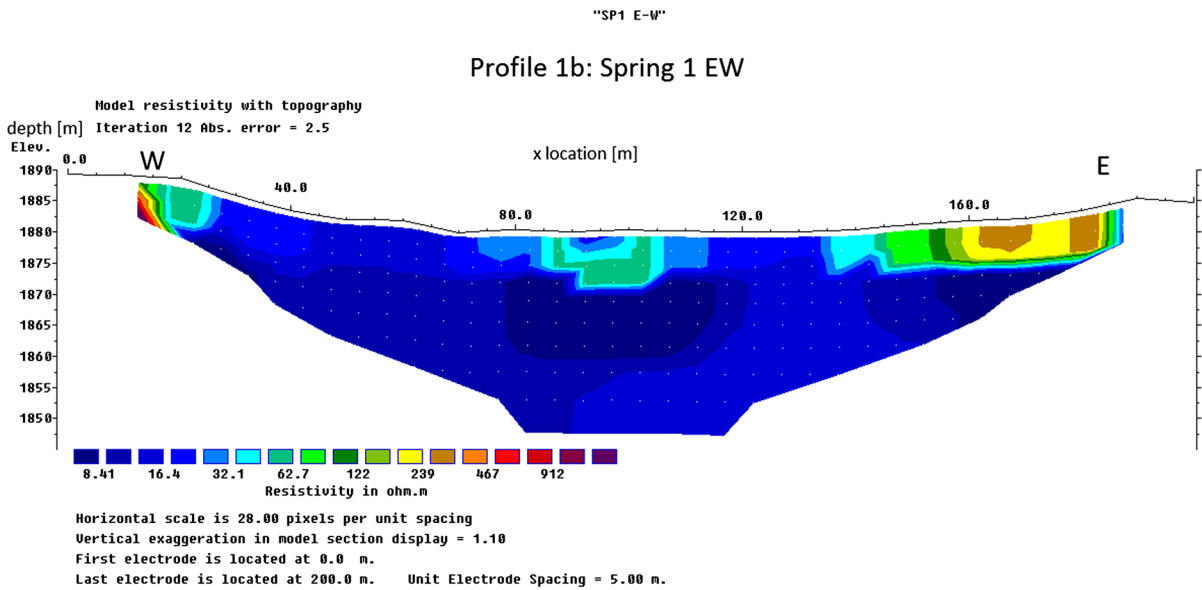2D resistivity model of profile 1a, Spring 1, North–South

"SP1 E-W"

## Profile 1b: Spring 1 EW

Model resistivity with topography
depth [m] Iteration 12 Abs. error = 2.5

x location [m]

Horizontal scale is 28.00 pixels per unit spacing
Vertical exaggeration in model section display = 1.10
First electrode is located at 0.0  m.
Last electrode is located at 200.0 m.    Unit Electrode Spacing = 5.00 m.

Figure 7
2D resistivity model of profile 1b, Spring 1, East–West

SP2NS,,

## Profile 2a: Spring 2 NS

Model resistivity with topography
depth [m] Iteration 7 Abs. error = 3.3

x location [m]

Horizontal scale is 28.00 pixels per unit spacing
Vertical exaggeration in model section display = 1.10
First electrode is located at 0.0  m.
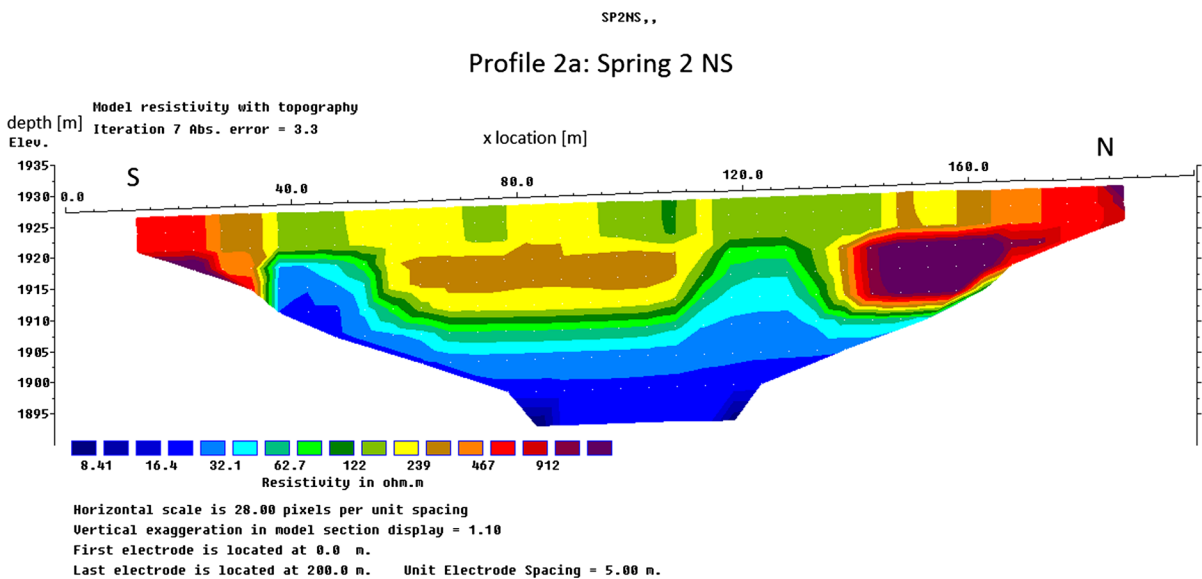Last electrode is located at 200.0 m.    Unit Electrode Spacing = 5.00 m.

Figure 8
2D resistivity model of profile 2a, Spring 2, North–South

have the highest signal strength perpendicular to the desired profile direction. The profile direction and direction of propagation must be perpendicular to have a good induction effect (McNeill and Labson 1991).

### 3.3. Data Processing and Interpretation

#### 3.3.1 I- 2D ERT

The 2D resistivity data were inverted using RES2DINV (Geotomo Software 2010). The inversion
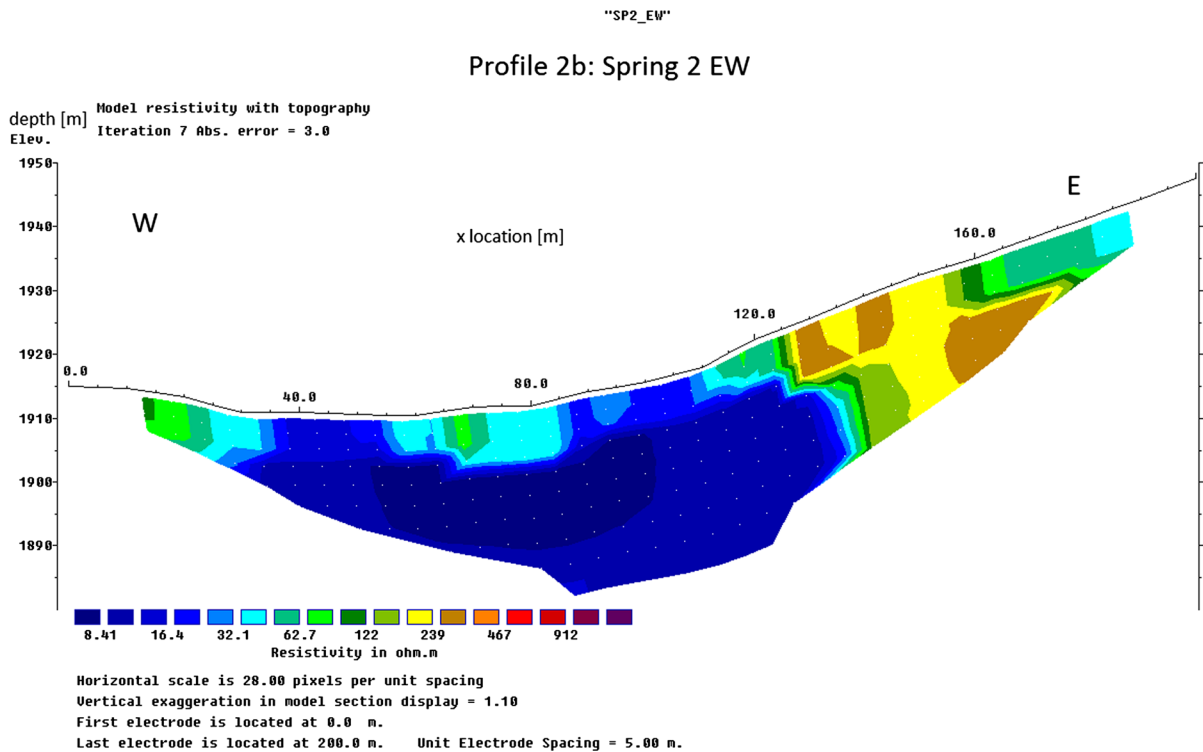
"SP2_EW"

## Profile 2b: Spring 2 EW



Figure 9
2D resistivity model of profile 2b, Spring 2, East–West

code is based on the smoothness-constrained least-squares method (Sasaki 1989, 1992, Loke 1995, Loke and Barker 1996a, 1996b). The operator is given the choice of using many methods such as the quasi-Newton method, which is the fastest in terms of inversion time, Gauss–Newton method (slower but increased accuracy), and a moderately fast hybrid technique which incorporates the advantages of the quasi-Newton and Gauss–Newton methods (TerraPlus 2013). The forward resistivity calculations were executed by applying a finite-difference method based on Dey and Morrison (1979). The first step in the inversion process is discretization of the model space. During this inversion, a multiple layers earth model was used as the starting model. This initial model was modified iteratively to reduce the root-mean-squared (RMS) error of the difference between the model response and the observed data (Loke 1995). Minimizing RMS error to its lowest possible value (potentially overfitting the model) sometimes results in large variations in resistivity that are not

realistic from a geological perspective. A better approach is to choose the model at the iteration after which the RMS error does not change significantly. We used L1 norm smoothness constrained optimization method. This is more commonly known as a blocky model inversion method or robust method. The robust inversion method has been recommended if the subsurface resistivity has sharp boundaries (Loke 1995), which is the case in our study.

The approximately north–south trending profile at spring 1 is characterized by two geoelectric zones (Figs. 5 and 6). The first zone to the north is characterized by high resistivity values (around 400 Ω m). The second zone to the south has a low resistivity (< 20 Ω m). From this profile, we see a sub-horizontal discontinuity located roughly 110 m from the first electrode. This discontinuity is located at the approximate location of Spring 1. The break in slope, the existence of a spring, and a change in soil types at this location strongly support this result. We interpret the discontinuity in the resistivity values to

be a contact between altered volcanic ash (clay; low resistivity) and basalt (high resistivity).

The approximately east–west oriented profile at spring 1 (Figs. 5 and 7) shows that the resistivity is relatively low (< 20 Ω m) and consistent; indicative of only minor changes in lithology in the subsurface. We interpreted this profile to be underlain by altered volcanic ash, with basalt near the surface on the east and west ends.

The approximately north–south striking profile near spring 2 (Figs. 5 and 8) shows a decrease in resistivity with depth, potentially caused by lithological variations in the subsurface. We interpret this to show altered ash overlain by basalt. There appear to be fracture zones in the basalt at about 40 and 120 m from the first electrode.

The approximately east–west striking profile at spring 2 (Figs. 5 and 9) shows high resistivity values near the surface at the east end and there is a marked reduction in resistivity values at approximately 120 m from the first electrode. We interpret this abrupt transition as a contact between basalt (high resistivity) and altered volcanic ash (clay; low resistivity). It is notable that the east–west trending profile at spring 2 is quite similar to the north–south striking profile at spring 1.

### 3.3.2 II- VLF-EM

Several analog and numerical methods have been developed to interpret VLF-EM data. The processing techniques most commonly employed for qualitative
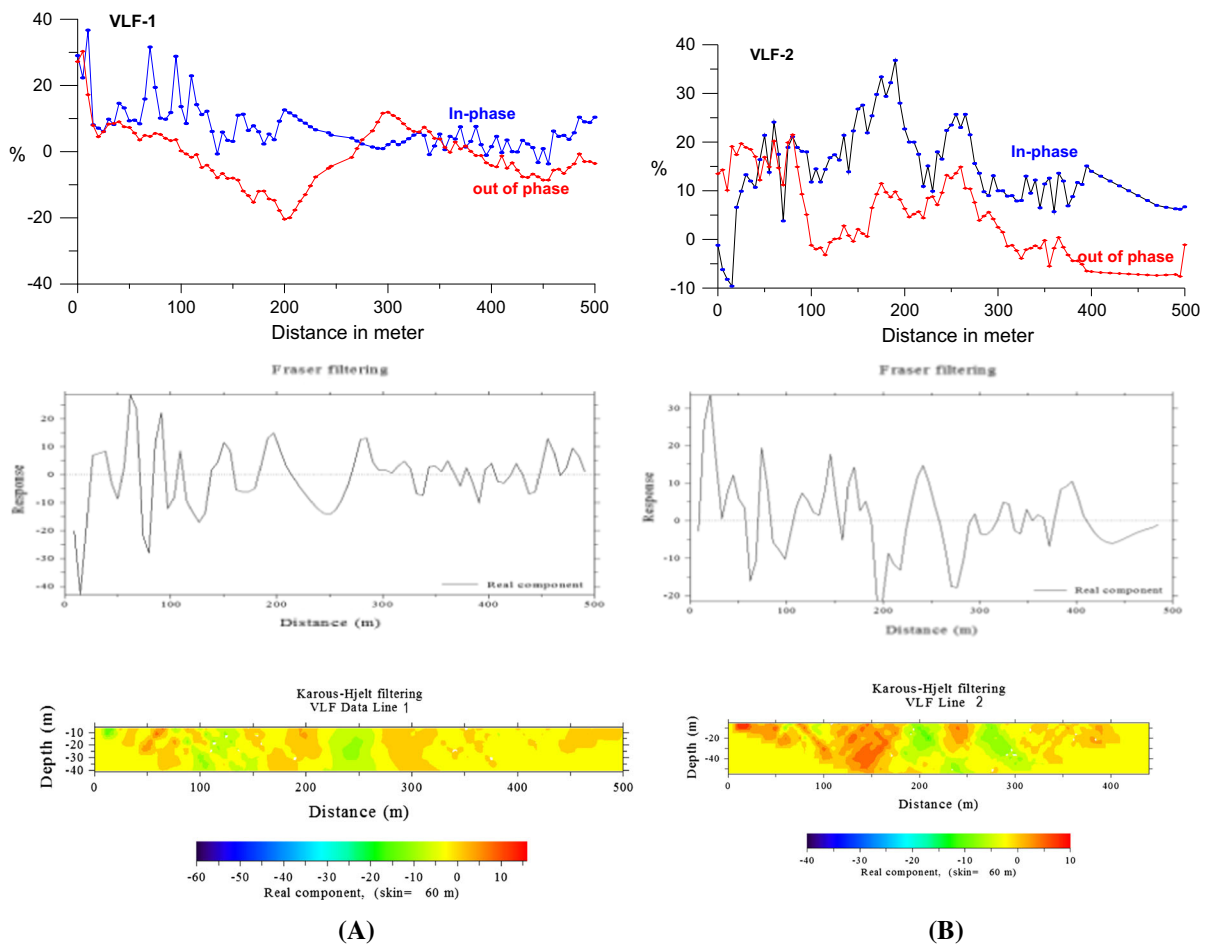


Figure 10
**a** the measured data (in phase and out of phase), Fraser filter, and K-H filter of the first line VLF-1, and **b** for the second line VLF-2
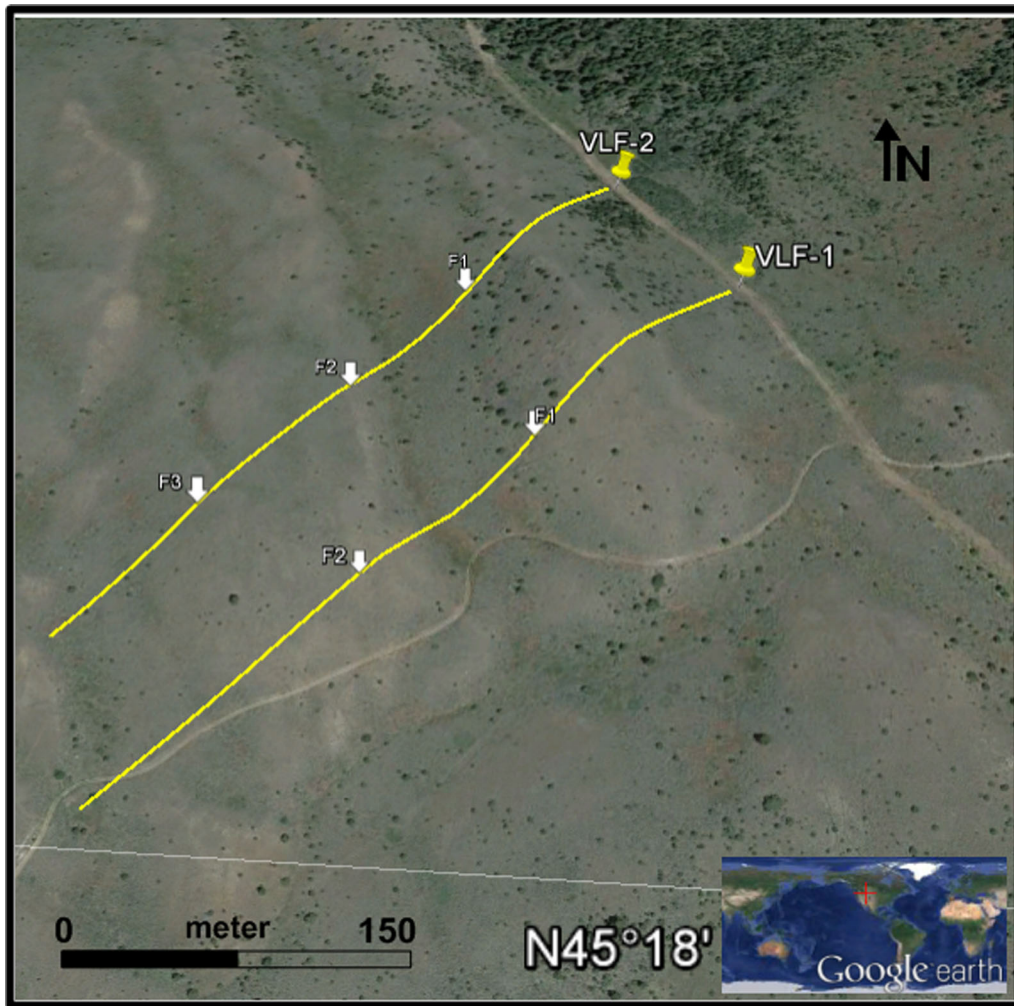
Figure 11
Location of VLF-1 and 2, and the observed high current density zones (F1, F2, and F3)

interpretation are Fraser (Fraser 1969) and Karous–Hjelt filters (Karous and Hjelt 1977, 1983). Fraser and Karous–Hjelt filters were used in this study to process and interpret the two VLF-EM profiles.

The Fraser filter (Fraser 1969) is functional to the tilt angle of the magnetic polarization ellipse (real component). The Fraser filter calculates horizontal gradients and smoothes the data to give maximum values over conductors that can then be contoured. Fraser filtering is effectively the first derivative of the data. The formula for Fraser filtering (Eq. 1), was applied on each set of four successive data points ($f_1$, $f_2$, $f_3$, and $f_4$):

$$(f_1 + f_2) - (f_3 + f_4) = F_{2,3} \qquad (1)$$

The resulting value ($F_{2,3}$) is plotted midway between the $f_2$ and $f_3$ points. The Fraser filter: (1) completely removes DC bias and greatly attenuates long wavelength signals; (2) completely removes Nyquist frequency related noise; (3) phase shifts all frequencies by 90°; and (4) has the band-pass bandwidth centered at a wave length that is five times the station spacing. Fraser filtering converts somewhat noisy and non-contourable in-phase components to less noisy and contourable data, which greatly improves the utility of the VLF-EM survey.
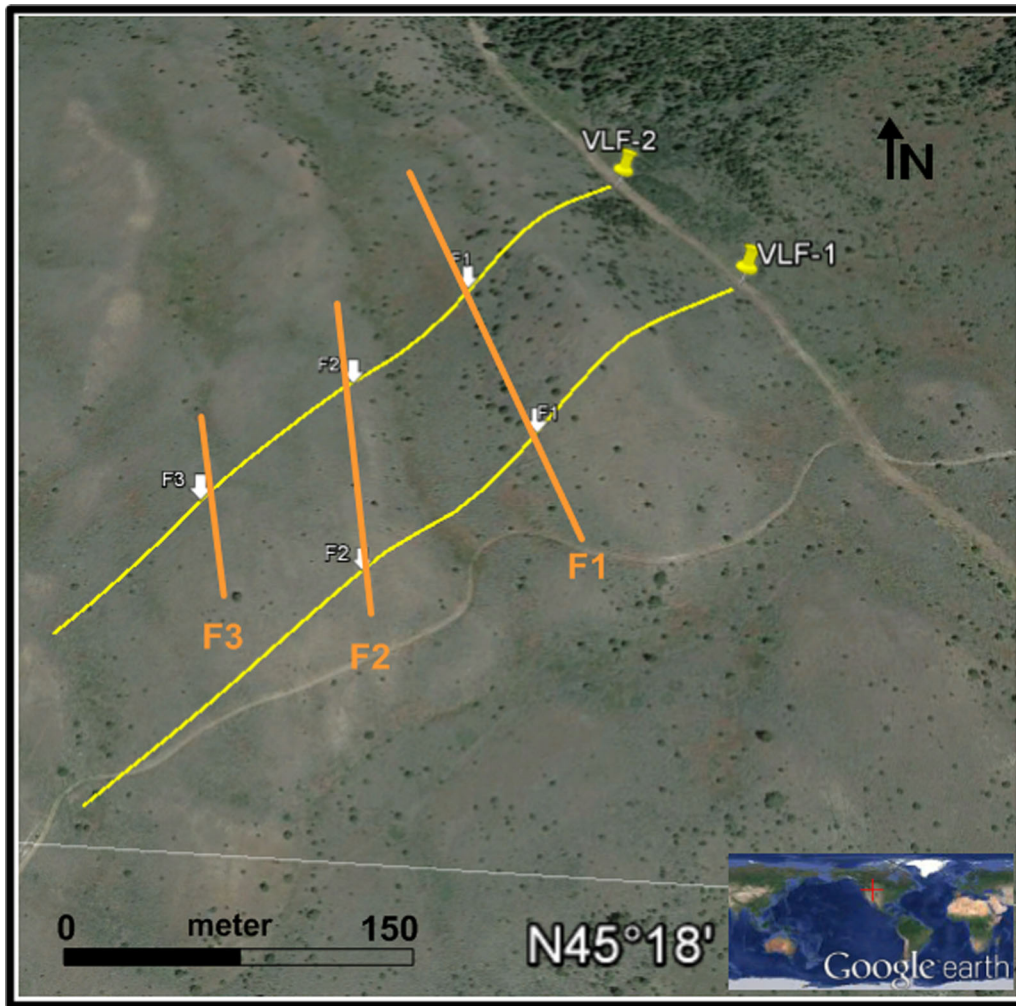
Figure 12
Skewed satellite image showing the surface trace of landslide scarps (orange lines) interpreted in the VLF profiles

The Karous and Hjelt filter (1977, 1983) generates an apparent current density pseudosection by filtering the in-phase data. The current density pseudosection manifests the apparent current concentrations at different depths, and approximates the spatial distribution of the conductor in the *X–Z* plane. Lower values of apparent current density correspond to higher values of resistivity, while high apparent current density corresponds to low resistivity (i.e. conductive minerals or a highly fractured saturated zone). In the simplest form, the Karous–Hjelt filter is:

$$\frac{\Delta z}{2\pi}I_a(\Delta x/2) = -0.205H_{-2} + 0.323H_{-1} - 1.446H_0$$
$$+ 1.446H_1 - 0.323H_2 + 0.205H_3 I_a(x/2)$$

(2)

where,

$\Delta Z$ is the assumed thickness of the current sheet,

$I_a$ is the current density,

$x$ is the distance between the data points and also the depth to the current sheet.

$H_{-2}$ through $H_3$ are the normalized vertical magnetic field anomaly at each of the six data points.

This filter shows the depth of the various current concentrations and hence the spatial dispositions of
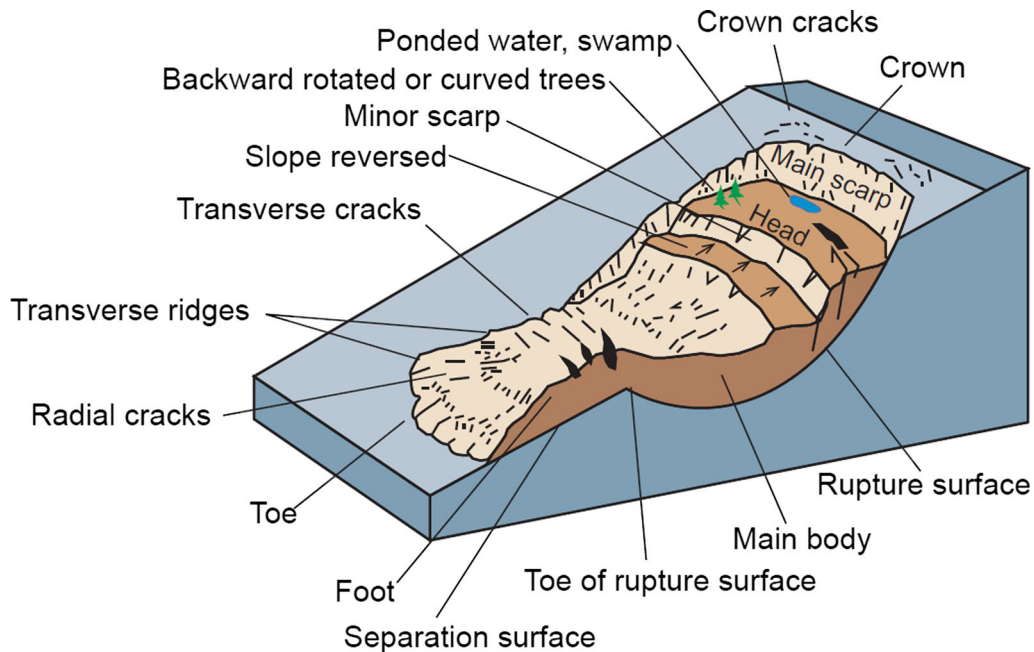
Figure 13
A schematic diagram of a rotational landslide (from Vuke 2013)

subsurface geological features, such as mineral veins, faults, shear zones and stratigraphic conductors (Ogilvy and Lee 1991). The finite Karous–Hjelt filter method is a more generalized and rigorous form of the widely known Fraser filter. However, the Karous–Hjelt filter is derived directly from the concept of magnetic fields associated with the current flow in the subsurface.

The Fraser and Karous–Hjelt filters were applied to the two measured VLF-EM profiles, using software developed by Pirttijarvi (2004) (Fig. 10). The Karous–Hjelt filter was applied based on a skin depth of 60 m. This skin depth was estimated using the transmitter frequency (24.7 kHz) and the environmental resistivity (400 Ω-m) from the 2D resistivity section.

The Karous–Hjelt filter of profile VLF-1 shows high current density (hot color) at about 180 and 300 m from the beginning of the section. We interpret these areas of high current density to show fracture zones near landslide scarps. Similar high current density zones were observed in profile VLF-2 at distances of 150, 250, and 380 m from the beginning of the section (Figs. 10 and 11). Assuming that these zones are connected, they show fracture

zones running sub-parallel to the landslide pressure ridges.

## 4. Discussion and Interpretation

ERT results, field observations, and previous geologic mapping of the area (Ruppel and Liu 2004; Kellogg and Williams 2006) indicate that the higher resistivity geoelectric layers in the ERT profiles most likely represent basalt flows, and the low resistivity geoelectric layers likely represent devitrified volcanic ash. At both springs there is a distinct contact between the ash unit and the overlying basalt, which is coincident with the location of the spring. At spring 1 clear evidence of mass movement suggests that this contact represents a landslide scarp. At spring 2 it is unclear if there was any movement along the contact; it may be a scarp, or it may be a depositional contact.

Anomalies in the Karous–Hjelt diagrams show zones of high apparent current density in both VLF-EM profiles. We interpret these zones as linear fracture zones corresponding to minor scarps in the landslide deposits (Figs. 12 and 13).

## 5. Conclusions

VLF-EM and ERT results help to characterize the hydrogeologic framework underpinning Virginia City's springs. Distinct discontinuities show an abrupt change in resistivity values in the ERT profiles, and we interpret these discontinuities to represent the contact between basalt and the underlying devitrified ash. The VLF-EM survey provides evidence for a series of fracture zones along minor scarps. The secondary permeability in these fracture zones likely provides a preferred pathway for water to flow towards spring 1, and may explain why spring 1 produces about six times as much water as spring 2. These fracture zones could also be targets for future water supply wells.

### REFERENCES

Burger, H. R., Sheehan, A. F., & Jones, C. H. (2006). *Introduction to Applied Geophysics*. New York: Norton.

Cordua, W. S. (1973). Precambrian geology of the southern Tobacco Root Mountains, Madison County. Montana: Bloomington, Ind., Indiana University, Ph.D. Thesis, p. 147.

Dahlin, T., Bernstone, C., & Loke, M. H. (2002). A 3D resistivity investigation of a contaminated site at Lernacken, Sweden. *Geophysics, 67,* 1692–1700.

Dey, A., & Morrison, H. F. (1979). Resistivity modelling for arbitrary shaped two-dimensional structures. *Geophysical Prospecting, 27,* 1020–1036.

Forquet, N., & French, H. K. (2012). Application of 2D surface ERT to on-site wastewater treatment survey. *Journal of Applied Geophysics, 80,* 144–150.

Fraser, D. C. (1969). Contouring of VLF-EM data. *Geophysics, 34,* 958–967.

Geotomo Software (2010). RES2DINV ver. 3.59 rapid 2-D resistivity and IP inversion using the least-squares method. Penang, Malaysia.

James, J. L. (1990). Precambrian geology and bedded iron deposits of the southwestern Ruby Range, Montana: U.S. Geological Survey Professional Paper 1495, p. 39

Karous, M., & Hjelt, S. E. (1977). *Determination of apparent current density from VLF measurements. Contribution N. 89.* Finland: Department of Geophysics, University of Oulu.

Karous, M., & Hjelt, S. E. (1983). Linear filtering of VLF dip-angle measurements. *Geophysical Prospecting, 31,* 782–794.

Kellog, K. S., & Williams, V. S. (2006). *Geologic Map of Ennis 30' x 60' Quadrangle Madison and Gallatin Counties, Montana, and Park County, Wyoming*. Butte: Montana Bureau of Mines and Geology.

Khalil, et al. (2010). Comparative study between filtering and inversion of VLF-EM profile data. *Arabian Journal of Geosciences.* https://doi.org/10.1007/s12517-010-0168-4.

Loke, M. H. & Barker, R. D. (1995). Least-squares deconvolution of apparent resistivity pseudocetions. *Geophysics, 60*(6), 1682–1690. https://doi.org/10.1190/1.1443900.

Loke, M. H., & Barker, R. D. (1996a). Rapid least-squares inversion of apparent resistivity pseudosections by a quasi-Newton method. *Geophysical Prospecting, 44,* 131–152.

Loke, M. H., & Barker, R. D. (1996b). Practical techniques for 3D resistivity surveys and data inversion. *Geophysical Prospecting, 44,* 499–523.

Madsen, J.A., Brown, L., McKenna, T., Snyder, S., Krantz, D., Manheim, F., Haeni, F.-P., White, E., Ullman, W. (2001). Geophysical characterization of fresh and saline water distribution in a coastal estuarine setting.In Proc. Symp. of the Application of Geophysics to Engineering and Environmental Problems (SAGEEP), 4–7 March, Denver, CO.

Manheim, F. T., Krantz, D. E., Snyder, D. S., Bratton, J. F., White, E. A., & Madsen, J. A. (2001). *Streaming resistivity surveys and core drilling define groundwater discharge into coastal bays of the Delmarva Peninsula Geological Society of America Annual Meeting, 33,* A42.

Marvin, R. F., Wier, K. L., Mehnert, H. H., & Merritt, V. M. (1974). K-Ar ages of selected Tertiary igneous rocks in southwestern Montana: Isochron West, n. 10, p. 17–20.

McNeill, J. D., Labson. V. F. (1991). Geological mapping using VLF radio fields (Chap. 7). In M.N. Nabighian (Ed.), *Electromagnetic methods in applied geophysics–Applications* (Vol. 2, Part B, pp. 521–640). Society of Exploration Geophysicists, ISBN 1-560800-22-4 (v.2).

Moeck, I., Dussel, M., Troger, U., & Schandelmeier, H. (2003). Fracture networks in Jurassic carbonate of the Algarve basin (south Portugal): Implications for aquifer behavior related to the recent stress field. In J. Krasny & J. Sharp (Eds.), *Groundwater in Fractured rocks*. Milton Park: Taylor and Fracis. **(ISBN 978-0-415-41442-5)**.

Monteiro Santos, F. A., Mateus, A., Figueiras, J., & Gonçalves, M. A. (2006). Mapping groundwater contamination around a landfill facility using the VLF-EM method – A case study. *Journal of Applied Geophysics, 60,* 115–125.

Ogilvy, R. D., & Lee, A. C. (1991). Interpretation of VLF-EM in phase data using current density pseudosections. *Geophysical Prospecting, 39,* 567–580.

Pirttijarvi, M. (2004). KHFFILTL Karous-Hjelt and Fraser filtering of VLF Measurements. Retrieved from https://wiki.oulu.fi/pages/viewpage.action?pageId=20677906. Accessed 13 May 2017.

Qarqori, K. H., Rouai, M., Moreau, F., Saracco, G., Dauteuil, O., Hermitte, D., et al. (2012). Geoelectrical Tomography Investigating and Modeling of Fractures Network around Bittit Spring (Middle Atlas, Morocco). *International Journal of Geophysics*. https://doi.org/10.1155/2012/489634. **(Article ID 489634)**.

Rizzo, E., Colella, A., Lapenna, V., & Piscitelli, S. (2004). High-resolution images of the fault-controlled high agri valley basin (Southern Italy) with deep and shallow electrical resistivity tomographies". *Physics and Chemistry of the Earth, 29*(4–9), 321–327.

Ruppel, E. T., & Liu, Y. (2004). *The Gold Mines of the Virginia City Mining District, Madison County* (p. 133). Montana Bureau of Mines and Geology Bulletin: Montana.

Sasaki, Y. (1989). Two-dimensional joint inversion of magnetotelluric and dipole–dipole resistivity data. *Geophysics, 54,* 254–262.

Sasaki, Y. (1992). Resolution of resistivity tomography inferred from numerical simulation. *Geophysical Prospecting, 40,* 453–464.

TerraPlus (2013). RES2DINV 2D resistivity and IP inversion software. TerraPlus—geophysical equipment supplier. http://terraplus.ca/products/resistivity/res2d.aspx

Tonkov, N., & Loke, M. H. (2006). A resistivity survey of a burial mound in the 'Valley of the Thracian Kings'. *Archaeological Prospection, 13,* 129–136.

Vuke, S.M., (2013). Landslide map of the Big Sky area, Gallatin and Madison counties, Montana: Montana Bureau of Mines and Geology Open-File Report 632, 1 sheet, scale 1:24,000.

Western Regional Climate Center (2017). https://wrcc.dri.edu/. Accessed 6 Sep 2017.

Wooden, J. L., Vitaliano, C. J., Koehler, S. W., & Ragland, P. C. (1978). The late Precambrian mafic dikes of the southern Tobacco Root Mountains, Montana. *Canadian Journal of Earth Sciences*, *15*, 467–479.

Wynn, J. C., & Grosz, A. E. (2000). Induced-polarization—a tool for mapping titanium-bearing placers, hidden metallic objects, urban waste on and beneath the seafloor. *Journal of Environmental and Engineering Geophysics, 5,* 27–35.